Band alignment at the CaF$_2$/Si(111) interface through advanced electronic structure calculations

Thomas Bischoff,[*] Igor Reshetnyak ⬤, and Alfredo Pasquarello ⬤

Chaire de Simulation à l'Echelle Atomique (CSEA), Ecole Polytechnique Fédérale de Lausanne (EPFL), CH-1015 Lausanne, Switzerland

We determine the band alignment at the CaF$_2$/Si(111) interface through various advanced electronic structure methods. This interface is experimentally well studied and serves as an ideal test case to examine the accuracy of theoretical schemes. We use both global and range-separated hybrid functionals as well as *GW* calculations including self-consistency and vertex corrections. Our calculation procedure accounts for residual strain resulting from the small mismatch in the lateral lattice constants at the interface to minimize the systematic error in the comparison with experiment. Both the hybrid functional and the *GW* schemes give band alignments in overall good agreement with the experimental characterization. However, the considered methods yield sizable variations in the calculated band offsets, which do not originate from incorrect evaluations of the band gaps but rather from different inherent relative positions of the band edges. The comparison with experiment reveals that the global hybrid functional and the quasiparticle self-consistent *GW* with vertex corrections give the most accurate description of the band alignment. We then determine the variation of the band offsets as a function of the amount of excess fluorine at the interface and attribute the experimental spread in the measured offsets to uncontrolled fluorine contamination.

I. INTRODUCTION

Insulator-semiconductor heterostructures are encountered in a broad variety of modern electronic devices. The precise understanding of their properties is of great practical importance [1]. However, an accurate theoretical description of such heterostructures is not trivial. It requires the appropriate prediction of the band gaps of the involved materials and the determination of their band alignment at the interface. The calculation of these quantities within density functional theory (DFT) in standard semilocal approximations [2,3] suffers from severe band-gap underestimations [4,5]. Advanced methods for electronic structure calculation like the many-body perturbation theory [6–9] and hybrid functionals [10–12] can overcome this deficiency and have therefore intensively been used for studying the interfacial band alignment [4,5,13–23]. It is worth noting that that these methods tend to position the band edges differently even when they give the same band gap [24–26]. This phenomenon is not yet fully understood and has direct implications on the prediction of band offsets in heterostructures [22].

For addressing this issue, it is necessary to determine band-edge positions with different electronic structure methods. However, band-edge levels from periodic bulk calculations cannot directly be compared with experimental references [24]. To circumvent this limitation, theoretical schemes have been examined through their accuracy in predicting ionization potentials at surfaces [9,27], band offsets at interfaces [22,23] or defect levels with respect to band edges [25,28]. While a comparison between theoretical schemes is relatively straightforward, the validation of the calculated band edges against

experimental data is more difficult. Indeed, the latter requires the availability of realistic structural models accounting for the detailed surface reconstruction [9] or the specific bonding pattern at interfaces [4,29]. In the absence of such models, it is an arduous task to draw conclusions concerning the quality of competing electronic structure methods.

In this context, the CaF$_2$/Si(111) interface can serve as an ideal test case. The CaF$_2$ layer is epitaxially grown on the silicon substrate [30] and the structural [31–37] and electronic [30,38–43] properties have been experimentally characterized in great detail. Furthermore, the combination of a semiconductor like Si with a wide band-gap insulator like CaF$_2$ leads to sizable band offsets. Therefore, differences between computational approaches are expected to be more pronounced than for heterostructures involving similar semiconductors [22,23].

In this work, we determine band offsets at the CaF$_2$/Si(111) interface using various advanced electronic structure schemes to examine their accuracy in comparison with the experimental characterization. Our investigation includes both hybrid-functional and *GW* calculations. In particular, we use both global and range-separated hybrid functionals and consider self-consistency and vertex corrections in the *GW* calculations. Our study also encompasses the effect of strain in the CaF$_2$ overlayer to ensure that it does not affect the comparison with experiment. In this way, we expect to be able to identify the most suitable theoretical approach for the band alignment. We then address the variation of the band offset upon the occurrence of extra fluorine at the interface.

This work is organized as follows. In Sec. II, we present the considered electronic structure methods and provide computational details of the calculations. Furthermore, we explain the adopted band-alignment scheme and discuss the role of strain effects in our modeling procedure. In Sec. III, we address bulk

*thomas.bischoff@epfl.ch

TABLE I. Computational parameters used throughout this work: **k**-point sampling, ground-state cutoff energy E_{cut}, cutoff energy E_{cut}^{eps} in the dielectric matrix, and total number of bands n_b (occupied and unoccupied) in the dielectric matrix and in the Green's function.

	k points	E_{cut} (Ry)	E_{cut}^{eps} (Ry)	n_b
Si bulk	$8 \times 8 \times 8$	60	15	300
CaF_2 bulk	$6 \times 6 \times 6$	100	30	500
CaF_2/Si interface	$8 \times 8 \times 1$	100		

TABLE II. Advanced electronic structure methods in this work: global (PBE0) and range-separated hybrid functionals (HSE); one-shot GW with ($G_0\tilde{W}_0$) and without (G_0W_0) vertex corrections using wave functions and energies either from PBE0 or from HSE; quasiparticle self-consistent GW with vertex corrections (QS$G\tilde{W}$). The inclusion of vertex corrections in the screening results in the notation $\tilde{W}$ for the screened Coulomb interaction. The notation with the parameter α indicates that the fraction of Fock exchange is adapted to match the experimental band gap.

Method	Global	Range separated
Hybrid functional	PBE0(α)	HSE(α)
One-shot G_0W_0	G_0W_0@PBE0(α)	G_0W_0@HSE(α)
One-shot $G_0\tilde{W}_0$	$G_0\tilde{W}_0$@PBE0(α)	$G_0\tilde{W}_0$@HSE(α)
QS$G\tilde{W}$		

materials and show their band gaps and band-edge positions relative to the average electrostatic potential. Section IV is devoted to the lineup of this potential at the CaF_2/Si(111) interface and to the discussion of the calculated band offsets. In Sec. V, we study the effect of interfacial Si-F bonding on the band offsets. We draw conclusions in Sec. VI.

II. METHODS

A. Advanced electronic structure calculations

In this work, we use various advanced electronic structure methods for determining the band alignment at the CaF_2/Si(111) interface. To this end, we perform calculations for the bulk components and for an interface model, as further explained in Sec. II B. First, we consider hybrid functionals [10–12,44] which show an improved description of band gaps [26] and offsets [4] compared to standard semilocal functionals. In particular, we investigate global as well as range-separated hybrid functionals. For the former, we use the functional PBE0(α), which depends on the amount of incorporated Fock exchange α [11]. For the latter, we consider the functional HSE(α, μ) which additionally includes a range-separation parameter μ [12,44]. For the purpose of this study, it is sufficient to vary only the mixing parameter α whereas μ is kept equal to 0.11 bohr^{-1} [44]. We remark that both functionals revert to the semilocal Perdew-Burke-Ernzerhof (PBE) functional [3] when $\alpha = 0$. For all calculations, we use plane-wave basis sets and norm-conserving pseudopotentials to describe core-valence interactions [45,46]. Only the outermost shells are treated among the valence states for Si ($3s^2 3p^2$) and F ($2s^2 2p^5$). In the pseudopotential of Ca, we include semicore shells ($3s^2 3p^6 4s^2$) as these states have been shown to be important in a previous GW study [47]. For the bulk calculations, we adopt the well-known primitive unit cells of Si and CaF_2, respectively. More specifically, we model Si bulk with a face-centered-cubic (fcc) cell with two Si atoms located at the reduced coordinates $(0, 0, 0)$ and $(\frac{1}{4}, \frac{1}{4}, \frac{1}{4})$ [48]. CaF_2 bulk is described by a fcc lattice with one Ca atom at $(0, 0, 0)$ and two F atoms at $(\frac{1}{4}, \frac{1}{4}, \frac{1}{4})$ and $(-\frac{1}{4}, -\frac{1}{4}, -\frac{1}{4})$ [47]. The structural details of the interface models are given in Secs. IV A and V. The adopted **k**-point sampling and the energy cutoff are given in Table I. We verified that the adopted parameters ensure the convergence of the total energy of the ground state within 10^{-3} eV/atom. In the particular case of silicon, a dense **k**-point grid of $12 \times 12 \times 12$ is necessary to include the conduction-band minimum (CBM), which is not located at a high-symmetry **k** point [48]. To avoid using such a high-density grid in the more demanding electronic structure

schemes, we proceed in the following way. We first perform advanced and semilocal calculations with a coarser $8 \times 8 \times 8$ **k**-point mesh. The differences are evaluated and interpolated to match the denser $12 \times 12 \times 12$ **k**-point grid. The final results are achieved by combining the interpolated corrections with a PBE calculation on the $12 \times 12 \times 12$ **k**-point grid. This way of proceeding is appropriate since the energy corrections only weakly depend on the considered **k** point [49–51]. The final band gaps differ only by $\sim$0.04 eV with respect to the estimation achieved with the coarser $8 \times 8 \times 8$ **k**-point mesh.

As a second kind of advanced electronic structure method, we use many-body perturbation theory in the GW approximation [6]. This approach is often applied as a one-shot perturbative correction to the single-particle eigenvalues resulting in noticeably improved band gaps [22,26], ionization potentials [26], and band offsets [13–16,19–22]. In our work, we perform one-shot GW calculations to correct the single-particle energies obtained from hybrid functional calculations. In this way, the adopted GW method depends on the fraction of Fock exchange used in the preceding hybrid functional calculation. Furthermore, we consider self-consistency [7–9] and vertex corrections [9]. We account for vertex corrections through the use of the bootstrap exchange-correlation kernel [9,52]. The GW calculations are performed with nonlocal commutators for the optical matrix element in the long-wavelength limit as described in Ref. [53]. The dielectric function is calculated with the formula of Adler and Wiser [54,55], including an energy cutoff E_{cut}^{eps} and a total number of bands n_b as given in Table I. The frequency dependence of the dielectric function is evaluated through the contour deformation technique [56] accounting for 10 real and 10 imaginary frequencies. In the quasiparticle self-consistent GW (QS$G\tilde{W}$) approach [7,8], we only update the lowest 100 bands self-consistently and keep higher-lying states as obtained at the PBE level. The update of more bands leads to indiscernible changes in the band edges. Overall, we estimate that the quasiparticle energies are converged within 0.05 eV. A summary of the electronic structure methods investigated in this work is given in Table II.

All presented calculations for the bulk materials are carried out with the code ABINIT [57], whereas the interface calculations are performed with the QUANTUM ESPRESSO software package [58]. We use the same pseudopotentials in both cases
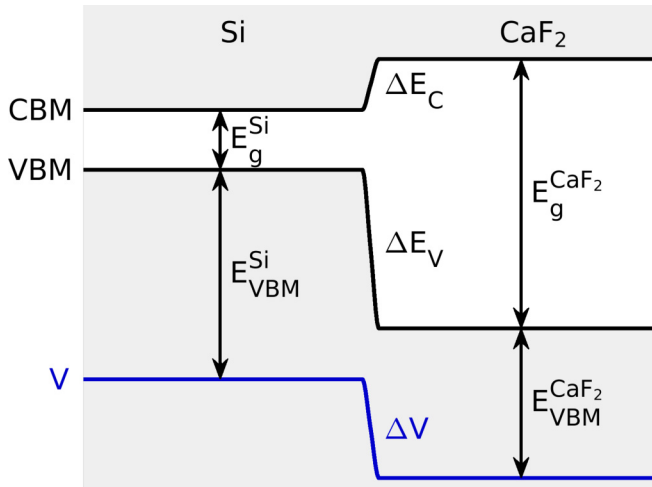
FIG. 1. Band-alignment scheme for the calculation of the valence-band offset $\Delta E_{\rm V}$ and of the conduction-band offset $\Delta E_{\rm C}$ at the CaF$_2$/Si(111) interface.

to ensure a meaningful combination of the results obtained with the two codes.

B. Band-alignment scheme

In this study, we determine the band alignment following the scheme outlined in Refs. [59,60]. A graphical representation is given in Fig. 1. The band-offset determination is based on two individual bulk and on one interface calculation. The bulk models are used to position the valence-band maximum (VBM) $E_{\rm VBM}$ of each component relative to the average electrostatic potential V. In the interface model, the lineup of the average electrostatic potential across the interface ΔV is achieved. The valence-band offset $\Delta E_{\rm V}$ is found through

$$\Delta E_{\rm V} = E_{\rm VBM}^{\rm Si} - E_{\rm VBM}^{\rm CaF_2} + \Delta V. \qquad (1)$$

The conduction-band offset $\Delta E_{\rm C}$ is then inferred from the consideration of the band gaps of the two interface components (cf. Fig. 1).

We apply this scheme to evaluate the band alignment obtained through different electronic structure methods following the specific procedure outlined by Alkauskas *et al.* [4]. First, we focus on the hybrid functionals, which contain a single undetermined parameter α. For each interface component, we empirically determine the optimal α for which the calculated band gap of the bulk matches its experimental counterpart. This scheme is preferred over nonempirical techniques for fixing the free parameter [61–63], as ensuring the correct band gaps of the interface components has been found to be critical for accurately estimating the band offsets [4]. In particular, we impose an indirect band gap of 1.17 eV [48] for Si and a direct band gap of 12.0 eV [64] for CaF$_2$. The latter condition is equivalent to enforcing an indirect gap of 11.7 eV. The optimal mixing parameters $\alpha_{\rm Si}$ and $\alpha_{\rm CaF_2}$ obtained in this way for the PBE0(α) and HSE(α) hybrid-functional forms are given in Table III.

The interfacial lineup is then computed with a hybrid functional defined by the mean of the mixing parameters pertaining to the two interface components [4]: $\bar{\alpha} = (\alpha_{\rm Si} + \alpha_{\rm CaF_2})/2$.

TABLE III. Optimal mixing parameters $\alpha_{\rm Si}$ and $\alpha_{\rm CaF_2}$ that reproduce the experimental band gap of Si and CaF$_2$, respectively. The mean value $\bar{\alpha} = (\alpha_{\rm Si} + \alpha_{\rm CaF_2})/2$ is used in the interface calculation for the determination of the lineup.

			G_0W_0@		$G_0\tilde{W}_0$@	
	PBE0	HSE	PBE0	HSE	PBE0	HSE
$\alpha_{\rm Si}$	0.12	0.25	0.00	0.00	0.05	0.07
$\alpha_{\rm CaF_2}$	0.40	0.56	0.30	0.38	0.77	0.87
$\bar{\alpha}$	0.26	0.40	0.15	0.19	0.41	0.47

This approach is meaningful because the interfacial lineup potential is almost independent of the mixing parameter [4,18,22]. In this way, the combination of bulk and interface calculations provides us with the band offsets corresponding to a given hybrid-functional form. We remark that recent work has proposed nonempirical procedures to determine a spatially dependent mixing parameter in heterostructures through the definition of local physical quantities [65,66]. Possibly, this could also be achieved through Koopmans' condition applied to localized probes [62,63,67]. However, the weak dependence of the potential lineup on the adopted hybrid functional ensures that the band offsets are only marginally affected by the adopted scheme.

Next, we consider the band alignment for the electronic structure methods based on GW calculations. These calculations are performed for the bulk models of the interface components. For the lineup in the one-shot GW schemes, we follow the same procedure as for the hybrid functionals since these GW schemes also depend on an underlying value of α for the starting point. A specific value $\bar{\alpha}$ is thus identified as the mean of the optimal mixing parameters of the bulk components given in Table III. Since the one-shot GW calculations do not modify the charge density, we use the lineup potential achieved with the hybrid functional defined by $\bar{\alpha}$. By contrast, in the QS$G\tilde{W}$ scheme, the band-gap determination does no longer depend on the value of α of the starting hybrid functional because of the iteration toward self-consistency. Therefore, a QS$G\tilde{W}$ calculation would in principle lead to a distinct value of the lineup ΔV. However, such high-level GW calculations are computationally demanding for large supercells and do not lead to any sizable variation in ΔV. Indeed, Shaltaf *et al.* [5] calculated for the Si/SiO$_2$ interface an effect of only 0.02 eV on ΔV due to the self-consistency. This property stems from the fact that QSGW only brings minor variations to the charge density and thus to the electric dipoles, as also seen in the case of small molecules [68]. In view of these considerations, we use in our QS$G\tilde{W}$ scheme the same value of ΔV as obtained with the hybrid functionals. In the QS$G\tilde{W}$ scheme, the band gaps do not match the experimental ones by construction. Hence, it should be considered that the band offsets could suffer from this drawback [4].

C. Strain effects

We now devote special attention to the strain in our description of the CaF$_2$/Si(111) interface. There are multiple reasons to properly account for such effects. First, in experimental

TABLE IV. Lattice constants (in Å) for Si and CaF_2 considered in this work. a_{bulk}^{Si} and $a_{bulk}^{CaF_2}$ are the experimental lattice constants of bulk Si and bulk CaF_2, respectively. $a_{layer}^{CaF_2}$ is the lattice constant in the growth direction for a CaF_2 layer epitaxially grown on Si, determined through the experimental Poisson ratio. a_{model}^{Si} and $a_{model}^{CaF_2}$ are lattice constants in the growth direction as found in the respective bulk regions of the relaxed model interface.

a_{bulk}^{Si}	a_{model}^{Si}	$a_{model}^{CaF_2}$	$a_{bulk}^{CaF_2}$	$a_{layer}^{CaF_2}$
5.431[a]	5.484	5.581	5.463[b]	5.587

[a]Reference [48].
[b]Reference [69].

conditions, the CaF_2 layer grows epitaxially upon silicon [30] with a residual mismatch, which causes this layer to be subject to compressive strain in the in-plane directions [30,38,39]. For the present interface, the experimental mismatch is particularly small and corresponds to 0.59% (cf. lattice constants in Table IV). Second, our interface modeling englobes a structural relaxation (cf. Sec. IV A), which leads the relaxed model interface to exhibit lattice constants in the growth direction that differ from the targeted experimental situation. Third, we have a preference for performing the advanced calculations on bulk systems, on the one hand to take advantage of the high symmetry, and, on the other hand, to establish benchmark results for future reference. Fourth, one of the motivations of this work consists in comparing different advanced electronic structure methods to experiment and it is thus important to reduce effects that could bias our conclusions as much as possible. Hence, the motivation for paying attention to strain effects arises from both experimental and computational conditions. In this section, we describe how these effects are accounted for.

We specifically distinguish between the lattice constants in the lateral directions a_{lat} and in the growth direction a_z. These quantities exhibit different values for bulk Si, bulk CaF_2, the interface model, and the strained CaF_2 layer in the experiment. A schematic illustration of the different configurations is shown in Fig. 2. Our ultimate intention is to calculate the alignment between unstrained silicon with experimental lattice constant a_{bulk}^{Si}, i.e. with $a_{lat} = a_{bulk}^{Si}$ and $a_z = a_{bulk}^{Si}$, and a CaF_2 layer that is strained because of the lattice mismatch, i.e., for which $a_{lat} = a_{bulk}^{Si}$ and $a_z = a_{layer}^{CaF_2}$. The value of $a_{layer}^{CaF_2}$ is determined through the experimental values for the mismatch and the Poisson ratio of CaF_2. For the latter, we here use the value of $\nu = 0.26$ from Refs. [70,71]. To achieve this goal, our band-alignment scheme takes advantage of (i) bulk calculations of Si and CaF_2 that are performed at their respective experimental bulk lattice constants, a_{bulk}^{Si} and $a_{bulk}^{CaF_2}$, and of (ii) an interface model calculation, in which the in-plane lattice constant is fixed at the target a_{bulk}^{Si}, but the a_z lattice constants of both components are allowed to relax according to the electronic structure scheme used, giving a_{model}^{Si} and $a_{model}^{CaF_2}$. The various lattice constants used in this work are compiled in Table IV.

To connect the two structural calculations of Si, we follow the scheme for evaluating deformation potentials proposed in Ref. [72]. We construct a superlattice in which regular Si
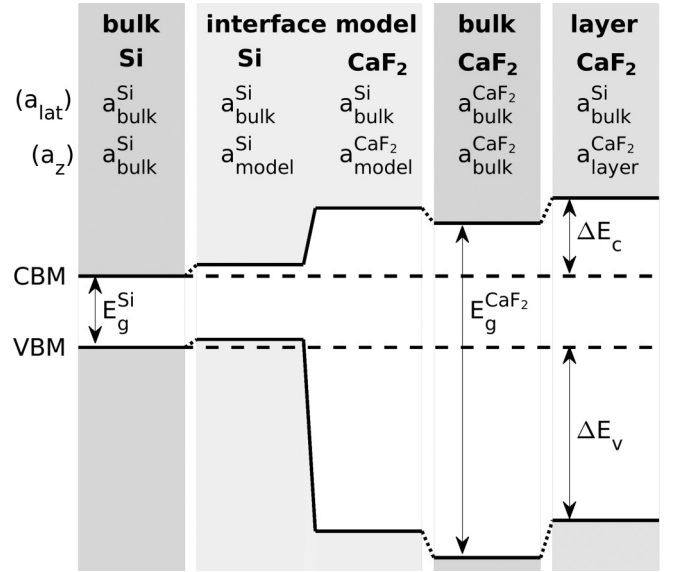

FIG. 2. Schematic illustration of the band alignment of bulk Si, Si, and CaF_2 within the interface model, bulk CaF_2, and the strained CaF_2 layer. The lattice constants in the lateral directions a_{lat} and in the growth direction a_z are indicated. The band gaps for Si and CaF_2 are shown in correspondence of the unstrained bulk configurations. The targeted valence-band offset ΔE_V and conduction-band offset ΔE_C, corresponding to those measured in the experimental conditions, are also indicated.

alternates with a Si layer in which the lattice constant along the growth direction has been modified. We obtain in this way a strain-induced shift in the electrostatic potential ΔV (Si bulk → Si model). For CaF_2, we proceed analogously. From a superlattice calculation between regular and strained CaF_2, we obtained the effect of uniaxial strain on the electrostatic potential and on the band edges. Based on the symmetry and the linearity in the strain, we then extend the results to the specific strain transitions between the three structural configurations of CaF_2 of interest to us. More specifically, we derive in this way ΔV(CaF_2 model → CaF_2 bulk) and the strain-induced band-edge shifts between bulk CaF_2 and the strained CaF_2 layer, i.e., ΔE_V(CaF_2 bulk → CaF_2 layer) and ΔE_C(CaF_2 bulk → CaF_2 layer). We perform these calculations with the hybrid-functional schemes PBE0(α) and HSE(α), i.e., with parameters α set as in the respective bulk phases (cf. Table III). The results obtained are reported in Table V.

We generally observe small effects due to strain, which is consistent with the epitaxial growth found for this interface [30]. More specifically, we find strain-induced shifts in the electrostatic potential of −0.10 and 0.25 eV for ΔV (Si bulk → Si model) and ΔV (CaF_2 model → CaF_2 bulk), respectively. For the potential lineup between bulk Si and bulk CaF_2 this yields an overall correction of only 0.15 eV with respect to the value obtained through the interface model. For the band-edge shifts between bulk CaF_2 and the strained CaF_2 layer, we find with PBE0(α) a shift of −0.16 and 0.09 eV for the VBM and CBM, respectively. The strain corrections calculated with HSE(α) differ by at most 0.01 eV. We expect corrections of similar size for the other electronic structure

TABLE V. Strain-induced shifts (in eV) of the electrostatic potential ΔV (Si bulk $\rightarrow$ Si model) and ΔV (CaF$_2$ model $\rightarrow$ CaF$_2$ bulk) and of the valence- and conduction-band levels ΔE_V (CaF$_2$ bulk $\rightarrow$ CaF$_2$ layer) and ΔE_C (CaF$_2$ bulk $\rightarrow$ CaF$_2$ layer), as obtained with the hybrid functionals PBE0(α) and HSE(α). These shifts are used for all electronic structure methods in this work.

	PBE0(α)	HSE(α)
ΔV(Si bulk $\rightarrow$ Si model)	-0.10	-0.10
ΔV(CaF$_2$ model $\rightarrow$ CaF$_2$ bulk)	0.25	0.25
ΔE_V(CaF$_2$ bulk $\rightarrow$ CaF$_2$ layer)	-0.16	-0.17
ΔE_C(CaF$_2$ bulk $\rightarrow$ CaF$_2$ layer)	0.09	0.08

methods considered in this work. In particular, we apply for the one-shot GW schemes identical strain corrections as obtained with the underlying hybrid functional. For the QS$G\tilde{W}$ scheme, we use the corrections as calculated with PBE0(α).

III. BAND GAPS AND BAND-EDGE LEVELS OF BULK MATERIALS

We first focus on the bulk materials and determine band gaps and band-edge levels with respect to the average electrostatic potential. We devote special attention to the direct or indirect nature of the band gaps. In particular, we consider the direct ($\Gamma \rightarrow \Gamma$) and the indirect ($X \rightarrow \Gamma$) band gap for CaF$_2$ to enable a meaningful comparison with experiment. A summary of the calculated band gaps is given in Table VI together with experimental data for the fundamental band gap. At the PBE level the well-known band-gap underestimation is apparent. The advanced electronic structure methods provide a more realistic description of the band gap even when the hybrid-functional parameter is set to the default value $\alpha = 0.25$ without applying any optimization. In particular, we observe that the PBE0(0.25) band gaps are generally larger than the HSE(0.25) ones, in accord with the analysis in Ref. [18]. The G_0W_0 corrections tend to level out this difference when the two hybrid functionals are used as starting points. The inclusion of vertex corrections in the G_0W_0 only yields a minor reduction of the band gap. Overall, QS$G\tilde{W}$ gives the best agreement with experiment, further supporting the high accuracy of this scheme for band-gap evaluations [7–9,75,76].

For a proper comparison with experiment, it is necessary to consider the band-gap renormalization due to phonons. For

Si this effect is found to be 0.06 eV [77]. For CaF$_2$, such an estimate is unavailable in the literature but a sizable effect on the order of $\sim$0.5 eV can be expected on the basis of the result of a similar ionic compound such as MgO [78,79]. In the band-offset calculations in which the calculated band gaps reproduce their experimental counterparts, we assume that phonon renormalization effects are implicitly accounted for through the empirical tuning of the hybrid-functional parameter α. This way of proceeding is justified as long as the phonon renormalizations affect the band edges in a similar way as the scaling of α. However, the effect of phonon renormalization should be kept in mind when assessing the accuracy of QS$G\tilde{W}$ since this scheme does not rely on any band-gap tuning.

The band gaps calculated here are in good agreement with other theoretical studies in the literature. For Si, there are numerous computational studies including the application of both hybrid-functional and GW calculations [4,5,8,9,18,22,26,61,80]. Within this variety of references, we particularly focus on the high-level GW calculations of Refs. [8,9]. These studies found QS$G\tilde{W}$ band gaps of 1.24 and 1.30 eV, respectively, in excellent agreement with our QS$G\tilde{W}$ result of 1.28 eV. For CaF$_2$, several studies based on the local density approximation (LDA) for the exchange-correlation energy report an indirect band gap ranging between $\sim$6.7 and 7.1 eV [47,73,81,82] These values agree well with our band gap of 7.33 eV obtained with the semilocal PBE functional. As for the more advanced electronic structure methods, we refer to the GW calculations of Ma and Rohlfing [82], the GW calculations of Shirley [73], and to the self-consistent screened-exchange LDA (sX-LDA) calculations of Kim *et al.* [81], which yield band gaps of 11.5, 11.38, and 11.66 eV, respectively. These results are all in good agreement with our QS$G\tilde{W}$ band gap of 11.47 eV.

We then turn to band-edge levels as obtained at the various levels of theory. Our hybrid-functional results are illustrated in Fig. 3, where the band-edge levels are displayed as a function of the hybrid-functional parameter α. We generally observe a linear dependence of the VBM and CBM on the fraction of incorporated Fock exchange. The corresponding band-gap opening is smaller for HSE(α) than for PBE0(α), in analogy with the results in Ref. [18]. The linearity in α is preserved when applying a one-shot GW correction, as also found in Ref. [80] for other materials. In QS$G\tilde{W}$ such dependence on the starting point is overcome through the iteration toward self-consistency. For CaF$_2$, all GW approaches provide almost

TABLE VI. Band gaps (in eV) for Si and CaF$_2$ as calculated at various levels of theory. It is specified whether the band gaps correspond to direct or indirect transitions. All the results in this table are obtained with hybrid functionals in which $\alpha = 0.25$. The experimental data refer to fundamental band gaps.

	PBE	PBE0(α)	HSE(α)	G_0W_0@			$G_0\tilde{W}_0$@			QS$G\tilde{W}$	Expt.
				PBE	PBE0(α)	HSE(α)	PBE	PBE0(α)	HSE(α)		
Si (indirect)	0.57	1.79	1.17	1.17	1.54	1.41	1.11	1.44	1.33	1.28	1.17[a]
CaF$_2$ (indirect)	7.33	10.11	9.30	10.41	11.51	11.28	9.28	10.07	9.98	11.47	11.8[b]
CaF$_2$ (direct)	7.58	10.37	9.57	10.72	11.80	11.57	9.59	10.37	10.28	11.76	12.0 $\pm$ 0.1,[c] 12.1[d]

[a]Reference [48], extrapolated to $T = 0$ K.
[b]Estimation of Shirley [73] based on Ref. [74].
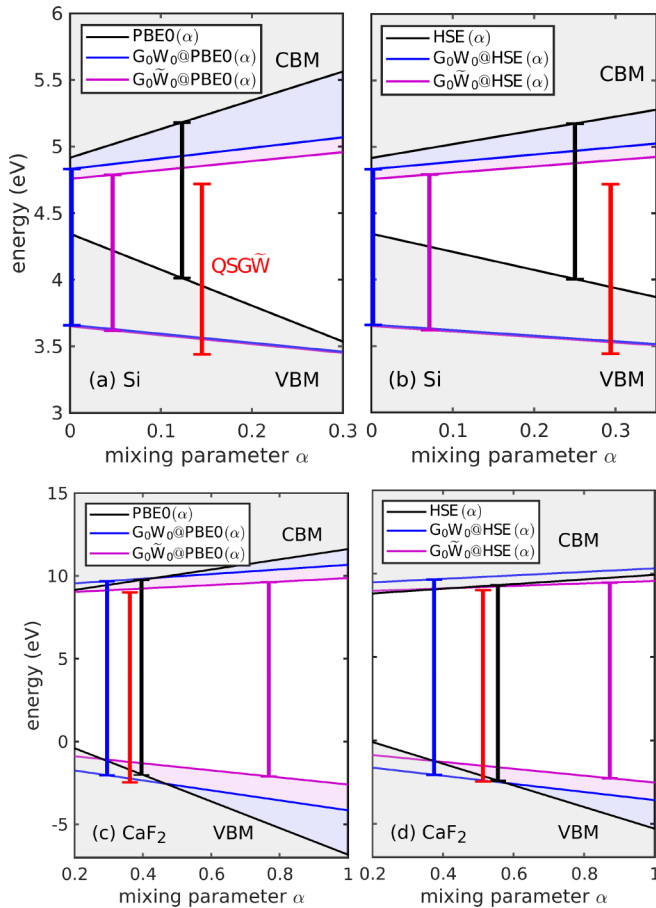[c]Reference [64], $T = 15$ K.
[d]Reference [74], $T = 90$ K.

FIG. 3. Band-edge levels (in eV) for Si and CaF_2 as calculated through various levels of theory. The VBM and the CBM are displayed as a function of the fraction of Fock exchange α. We show the results for Si as obtained with (a) the $PBE0(\alpha)$ and (b) the $HSE(\alpha)$ functionals. The results for CaF_2 are presented analogously in (c) and (d). The band-edge levels obtained with the one-shot GW methods are also given. The vertical bars indicate the value of α needed to reproduce the experimental band gap. The red bar highlights band edges as calculated with QS$G\tilde{W}$ and is positioned at the mixing parameter for which the hybrid functional and QS$G\tilde{W}$ give the same band gap. The energy levels are aligned through the average electrostatic potential.

symmetric band-edge corrections with respect to the hybrid-functional starting points, i.e., the upward shift of the CBM has a similar size to the downward shift of the VBM. Instead, for Si the VBM and CBM are both subject to a negative energy

correction. Our results are generally consistent with the finding of Chen and Pasquarello that different electronic structure methods tend to position the band edges differently [26]. This appears clearly when comparing the band edges from QS$G\tilde{W}$ with those from the hybrid functionals with optimal mixing parameters, as can be seen in Fig. 3 and Table VII. For Si, we observe that the valence-band edges as calculated with the hybrid functionals are persistently higher by 0.3 to 0.6 eV than corresponding ones in GW. For CaF_2, no such simple statement can be made. In this case, the most pronounced differences are found for the band edges obtained with the hybrid functionals. More specifically, the valence-band edge from $HSE(\alpha)$ is ~0.4 eV lower than that from $PBE0(\alpha)$. The GW approaches yield values lying in-between those obtained with the two hybrid functionals.

IV. BAND ALIGNMENT AT THE CaF₂/Si(111) INTERFACE

A. Interfacial lineup potential

For the calculation of the interfacial lineup potential ΔV, we use the so-called T_4 interface model in B-type orientation [30,83], which is characterized by a predominance of Si-Ca bonds at the interface. The interface is charge neutral and the Ca atoms are located at the T_4 sites of the Si(111)-(1 × 1) surface. We remark that the precise interface morphology has intensively been debated in the literature [30,31,34,38] resulting in clear evidence for the presently adopted T_4-interface model [32,35–37,42]. Furthermore, computational studies based on this model structure successfully accounted for photoemission [84,85] and second-harmonic generation measurements [83].

In our superlattice model, we use ~21 Å of Si and ~20 Å of CaF_2. We carefully check that such thicknesses ensure a bulklike electrostatic potential far from the interface. In order to mimic the epitaxial growth, the experimental lattice constant of Si is adopted for the lateral directions. We further find that the structural relaxation of the interfacial atomic positions has a significant influence on the lineup potential due to changes brought to the interface dipole. Therefore, we fully relax the structure at the PBE level until the total energy between two successive iteration steps is smaller than 10^{-5} Ry. The residual Hellmann-Feynman forces are then smaller than 10^{-4} Ry/bohr. In this structural optimization, we allow for the relaxation of both the atomic positions and the supercell size in the growth direction. The two other supercell dimensions are kept fixed. The model interface obtained in this way is used in all subsequent calculations of the interfacial lineup potential irrespective of the considered

TABLE VII. Valence band-edge levels (in eV) with respect to the average electrostatic potential for Si and CaF_2 as calculated at various levels of theory. The band-edge levels are expressed as shifts with respect to the reference PBE values at 4.35 and 1.21 eV for Si and CaF_2, respectively. Different calculations are aligned through the average electrostatic potential. For the parameter-dependent electronic structure methods, the fraction of incorporated Fock exchange α is tuned to reproduce the experimental band gap (cf. Table III).

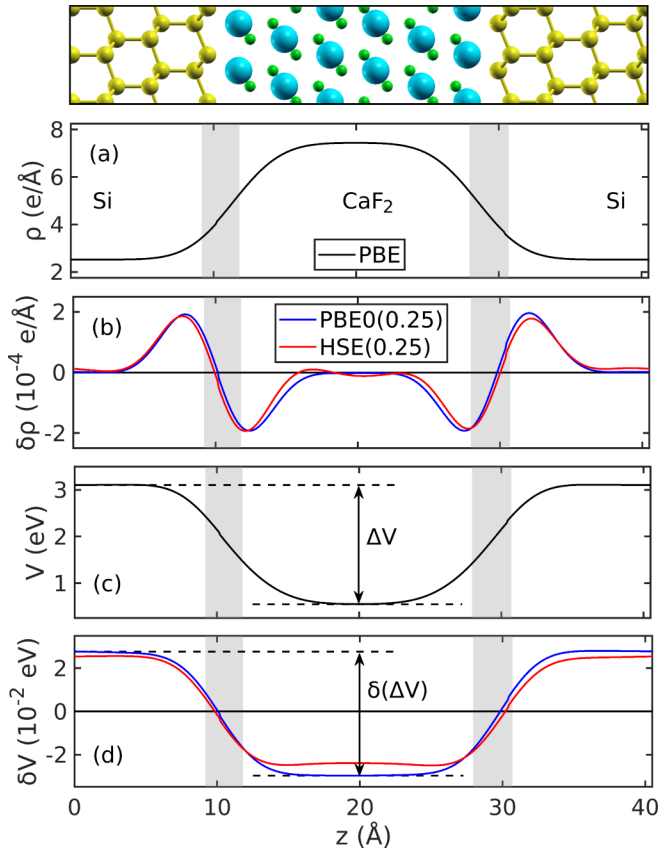|			$G_0W_0@$		$G_0\tilde{W}_0@$		
	$PBE0(\alpha)$	$HSE(\alpha)$	$PBE0(\alpha)$	$HSE(\alpha)$	$PBE0(\alpha)$	$HSE(\alpha)$	QS$G\tilde{W}$
Si	−0.33	−0.34	−0.68	−0.68	−0.73	−0.72	−0.90
CaF_2	−3.18	−3.61	−3.24	−3.26	−3.30	−3.47	−3.66

FIG. 4. Locally averaged (a) charge density ρ and (c) electrostatic potential V across the CaF$_2$/Si(111) interface as obtained with the semilocal PBE functional. (b) The charge density $\delta\rho$ and (d) the electrostatic potential δV as obtained with the hybrid functionals PBE0(0.25) and HSE(0.25) with respect to PBE are also given. The interfacial lineup ΔV in PBE and its modification $\delta(\Delta V)$ in the case of PBE0(0.25) are indicated. The shaded areas correspond to the transition regions between Si and CaF$_2$. In the top panel, the atomic structure of the interface model is illustrated: Si, Ca, and F atoms are shown in yellow, blue, and green, respectively.

level of theory. This is justified since structural relaxations at the hybrid-functional level only lead to minor changes. For instance, further relaxation with the functional PBE0(0.25) affects ΔV by 0.03 eV with respect to the value achieved with same functional but for the structure relaxed with the PBE functional. This is consistent with the results of Weston *et al.* [86].

We now study the lineup of the electrostatic potential at the CaF$_2$/Si(111) interface. To this end, we perform calculations for the constructed interface model at the various levels of theory considered in this work. We note that earlier studies demonstrated that electrostatic properties are already adequate at the semilocal DFT level [4,5,18,22]. Therefore, we first focus on the PBE level of theory. The corresponding charge density ρ and electrostatic potential V are given in Figs. 4(a) and 4(c), respectively. For simplicity, the displayed quantities are averaged in the lateral directions and broadened with a Gaussian of width 2.5 Å in the growth direction. We observe that ρ and V exhibit bulklike behavior away from the interfacial transition regions. From the difference between
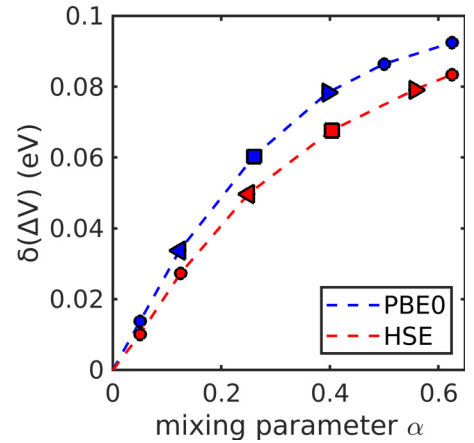

FIG. 5. Variation of the lineup potential $\delta(\Delta V)$ with respect to the result obtained with PBE as a function of the mixing parameter α in the hybrid functionals PBE0(α) and HSE(α). Calculations with the optimal mixing parameters for bulk Si and CaF$_2$ (cf. Table III) are shown as triangles pointing to the left and the right, respectively. Calculations with the mean of these mixing parameters are indicated with a square. Other calculated data points are shown with circles. Dashed lines are guides to the eye.

the plateau values in the electrostatic potential we infer a lineup potential of $\Delta V = 2.56$ eV at the PBE level. For the more advanced electronic structure methods, we focus on the differences in the charge density $\delta\rho$ and in the electrostatic potential δV with respect to PBE, as shown in Figs. 4(b) and 4(d), respectively. In particular, we display the results for the hybrid functionals PBE0(0.25) and HSE(0.25) as representative cases. We find that $\delta\rho$ and δV indeed correspond to minor modifications, namely, on the order of $\sim 2 \times 10^{-4}$ e/Å and ~ 0.03 eV, respectively. We observe a charge transfer from CaF$_2$ to Si [cf. Fig. 4(b)], which produces a change in the interfacial lineup potential $\delta(\Delta V)$ [cf. Fig. 4(d)]. This effect amounts to 0.06 eV for the functional PBE0(0.25). An almost identical value is found for the functional HSE(0.25).

To estimate the range of these deviations, we calculate $\delta(\Delta V)$ as a function of the hybrid-functional parameter α. The dependence is shown in Fig. 5 for both PBE0(α) and HSE(α). We find a linear dependence on α at low values, but a saturation becomes apparent at higher values. Overall, the variations in the lineup potential are generally smaller than 0.1 eV conferring consistency to the applied band-alignment scheme. To overcome the remaining dependence on the parameter, we follow the procedure outlined in Ref. [4]. This consists in using the lineup potential as calculated with the mean of the optimal mixing parameters of the bulk components (cf. Table III). For the hybrid functionals PBE0(α) and HSE(α), this yields almost identical lineup potentials of 2.62 and 2.63 eV, respectively. In the one-shot GW schemes, the lineup is obtained through the underlying hybrid functional defined with the mean value $\bar{\alpha}$ given in Table III. In the QS$G\tilde{W}$ scheme, we use the value of $\Delta V = 2.62$ eV obtained in PBE0(α) following the discussion in Sec. II B. These different choices for α lead to an uncertainty in the determination of ΔV that amounts to 0.05 eV at most.

TABLE VIII. Band offsets (in eV) for the $CaF_2/Si(111)$ interface as obtained at the various levels of theory considered in this work. Experimental data are given for comparison.

| | | | | $G_0W_0@$ | | $G_0\tilde{W}_0@$ | | | |
	PBE	PBE0(α)	HSE(α)	PBE0(α)	HSE(α)	PBE0(α)	HSE(α)	QS$G\tilde{W}$	Expt.
ΔE_V	5.73	8.58	9.01	8.28	8.31	8.31	8.48	8.49	8.7 ± 0.2[a]
ΔE_C	0.96	1.90	1.45	2.18	2.14	2.17	1.99	1.63	1.8 ± 0.2[b]

[a]References [38,39,43].

[b]Based on measured ΔE_V from Refs. [38,39,43] and the experimental band gaps considered in this work. The effect of strain in the CaF_2 overlayer is included through strain corrections determined at the PBE0(0.40) level (cf. Table V).

B. Band offsets at the interface

We now have all the ingredients for the calculation of the band offsets at the $CaF_2/Si(111)$ interface. For this we combine the band-edge positions determined in Sec. III with the interfacial lineup potential calculated in Sec. IV A. We also account for strain effects as discussed in Sec. II C. The band offsets obtained in this way are given in Table VIII, where they are compared with experimental data [38,39,43]. We remark that several differing experimental values for the band offsets can be found in the literature [30,38–43]. In Table VIII, we report an interval of experimental data that encompasses the three measurements with the highest values for the valence-band offset. We expect these results to be representative of the $CaF_2/Si(111)$ interface with a low contamination of Si-F bonds, as discussed in more detail in Sec. V.

All advanced electronic structure methods considered in this work yield a reasonable agreement with the experimental data showing errors of at most $\sim$0.4 eV, corresponding to only 3% of the largest band gap involved. In particular, the highest accuracy is found for the hybrid functional PBE0(α), which yields band offsets within $\sim$0.1 eV from the experimental ones. Interestingly, the high accuracy of the band alignment achieved in the PBE0(α) scheme has already been remarked previously in applications involving ionization potentials [80], band offsets at semiconductor heterostructures [22], and band alignments at solid-water interfaces [87]. At variance, the hybrid functional HSE(α) overestimates ΔE_V by $\sim$0.3 eV and hence underestimates ΔE_C by an equivalent amount. Among the GW methods, the QS$G\tilde{W}$ achieves the highest accuracy, resulting in both conduction- and valence-band offsets underestimated by $\sim$0.2 eV. This result is particularly remarkable because the band gaps are not empirically adjusted in the QS$G\tilde{W}$ scheme. However, the consideration of band-gap renormalization effects especially for CaF_2 might lead to a further deviation of the QS$G\tilde{W}$ band offsets with respect to the experimental ones (cf. Sec. III). For the one-shot GW methods, the agreement with respect to experiment is generally worse. In most cases, the valence-band offset is underestimated by $\sim$0.4 eV irrespective of the starting point and the use of vertex corrections. The only exception is found for $G_0\tilde{W}_0@$HSE, which yields band offsets of accuracy comparable with QS$G\tilde{W}$. All advanced electronic structure methods in this work overcome the band-gap problem encountered in the semilocal PBE approximation (cf. Table VIII) as well as in previous LDA-based schemes [88–90], which yield valence-band offsets underestimated by $\sim$2.0 to 2.4 eV.

Apart from the overall good agreement between theory and experiment, it is noteworthy to remark that the band offsets obtained with the various advanced electronic structure methods show sizable variations. These variations prevalently originate from the different positioning of the band-edge levels with respect to the average electrostatic potential (cf. Sec. III). The other ingredients of the modeling procedure, such as the potential lineup or the strain effects, cannot account for the size of the observed variations. At this point, it is of interest to identify which electronic structure method provides the most reliable description of the band-edge levels.

To address this issue, we focus on the two most accurate schemes, i.e., PBE0(α) and QS$G\tilde{W}$. The band offsets in these two schemes are very close (cf. Table VIII), but the band-edge levels are noticeably different. Indeed, the band-edge levels of both Si and CaF_2 calculated in QS$G\tilde{W}$ are deeper by 0.5–0.6 eV than the respective ones in PBE0(α). A similar situation occurs for interfaces between cubic semiconductors [22], which all belong to a similar class of materials from both the electronic and structural points of view. In the present case, this behavior is seen for two rather dissimilar materials exhibiting different crystal structure, degree of ionic bonding, and band gap. While this difference does not show up in the band offsets calculated here, it nevertheless directly affects the average electrostatic potential with respect to the vacuum level and in principle can be investigated through the comparison with experimental ionization potentials. In the case of the Si(111) surface, it has already been shown that the ionization potential calculated in the PBE0(α) scheme accurately reproduces the experimental value [80], whereas the QS$G\tilde{W}$ result shows a significant overestimation by about 0.5 eV [9]. For silicon, Grüneis et al. have shown that the consideration of higher-order diagrams in GW leads to an upward shift of about 0.3 eV [27], which would compensate the discrepancy to a noticeable extent. However, the same authors have shown that such a shift is not encountered for large band-gap materials and would thus presumably not apply to the case of CaF_2. Thus, it appears clearly that further investigations are necessary to understand the overall position of the band structure with respect to the average electrostatic potential or to vacuum level.

V. EFFECT OF INTERFACIAL Si-F BONDING

In this section, we address the reduction of the valence-band offset at the $CaF_2/Si(111)$ interface as the fraction of

Si-F bonding increases due to excess fluorine. The possibility of a Si-F termination has been amply discussed when determining the precise interface morphology [30–32,38]. While a predominance of Si-Ca bonds has clearly been identified at the interface [30,32,35–37,42,83,84], evidence for a certain percentage of Si-F bonds has also been established [30,33]. Despite the considerable efforts deployed [30,33,35,36,38,92], the quantitative dependence of the valence-band offset on the fraction of interfacial Si-F bonding has so far remained elusive.

Having established the accuracy of advanced electronic structure calculations, we are now in a suitable position for addressing this issue. For this purpose, we construct various interface models showing fractions of Si-F bonding corresponding to 25%, 50%, 75%, and 100% fluorine termination. To account for the intermediate fractions of fluorine termination, we double the size of the interfacial repeat unit used so far in both lateral directions, resulting in models with a total number of atoms multiplied by four. Following Refs. [30,39], we position the F atoms at the T sites of the Si(111)-(1 × 1) surface and the Ca atoms at the T$_4$ sites. In particular, for each of the intermediate percentages, we consider three interface models differing in the specific arrangement of Si-F and Si-Ca bonds. We apply the computational setup described in Sec. II, which includes a relaxation at the PBE level. We check that the considered percentages of Si-F bonds are preserved through the structural relaxation. The multiple structural models at the intermediate fractions show total energies differing by at most 0.7 eV per surface Si atom. In this way, the interface is described through a set of low-energy structural configurations. A shifted 2 × 2 × 1 **k**-point mesh is found to give converged lineup potentials. For the calculation of the band offsets, we use the hybrid functional PBE0(α), which has been shown in Sec. IV B to yield the highest accuracy among the electronic structure methods considered in this work.

The results of our study are illustrated in Fig. 6, in which the valence-band offsets are displayed versus the fraction of Si-F bonding. We observe a general reduction of the valence-band offset with increasing fraction of Si-F bonding. In particular, we determine a sizable difference of 4.7 eV between pure Si-Ca and pure Si-F bonding. When considering the various structural models at a given intermediate fraction, we find valence-band offsets falling in a range of ∼0.6 eV due to the varying bonding patterns. The descending trend of the valence-band offset is nevertheless well supported.

Our results demonstrate that the valence-band offset sensitively depends on the amount of interfacial Si-F bonding. In view of this dependence, we attribute the large spread from 7.0 to 8.8 eV in the experimental data [30,38–43,91,92] to different amounts of generally uncontrolled F contamination. On the basis of our calculations, we estimate that the utilized samples might contain up to 50% of Si-F bonding. In particular, in the experiment of Olmstead *et al.* [30], the fraction of Si-F bonding could be estimated resulting in a data point lying consistently with respect to the results of our calculations (cf. Fig. 6). This agreement supports the dependence found in Fig. 6.
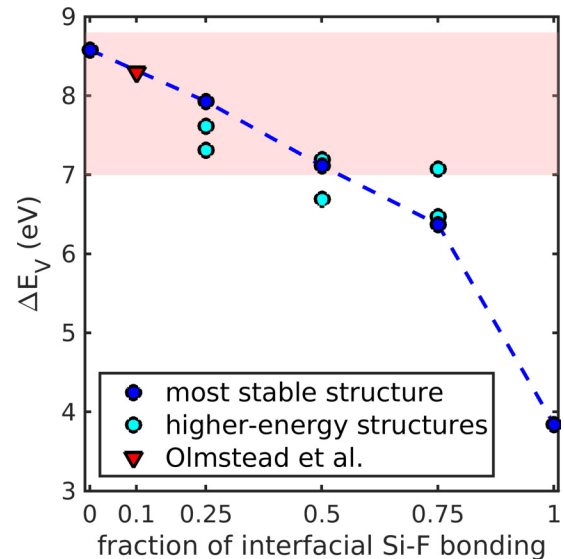

FIG. 6. Valence-band offset (in eV) versus the fraction of interfacial Si-F bonding. Calculated values are given as circles. The most stable and higher-energy structures are shown in blue and cyan, respectively. The dashed line is a guide to the eye. The shaded area indicates the interval of valence-band offsets measured in experiments in which the interfacial fraction of Si-F bonds has not been determined explicitly. The upper and lower bounds correspond to 8.8 eV [38] and 7.0 eV [91,92], respectively. The experimental result of Olmstead *et al.* [30] is illustrated with a red triangle at the estimated fraction of interfacial Si-F bonding.

VI. CONCLUSIONS

In this work, we investigated the band alignment at the CaF$_2$/Si(111) interface through various advanced electronic structure methods based on hybrid-functional and *GW* calculations. This allowed us to assess the accuracy of these theoretical schemes for an interface that has been extremely well characterized from the experimental point of view. In particular, we considered both PBE0(α) and HSE(α) hybrid-functional forms, several one-shot *GW* methods with various starting points, with or without vertex corrections, and the self-consistent QS*G$\tilde{W}$* scheme. All applied schemes were empirically tuned to reproduce the experimental band gap, with the only exception being the fully *ab initio* QS*G$\tilde{W}$*. We determined the band offsets by combining the band-edge levels calculated for the bulk components with the lineup of the average electrostatic potential at the interface.

All electronic structure methods considered in this work perform satisfactorily, yielding band offsets within 0.4 eV from the experimental values. The highest accuracy encountered is 0.1 eV and is found for the empirically tuned PBE0(α) hybrid functional. This result is particularly interesting since it further extends the range of successful applications of this scheme [22,80,87]. QS*G$\tilde{W}$* is the next most accurate scheme reproducing the experimental band offsets within 0.2 eV. This is particularly remarkable since the band gap of the interface components is not imposed in this scheme, but determined in a fully *ab initio* fashion.

Apart from finding an overall good agreement with experiment, our study reveals significant differences between the band offsets calculated with the applied electronic structure methods. Due to their size, the origin of these differences can be reconducted to the position of the band-edge levels with respect to the average electrostatic potential in each electronic structure scheme. In particular, it is interesting to compare PBE0(α) and QS$G\tilde{W}$. While both schemes give band offsets agreeing within at most 0.2 eV with the experiment, the band edges with respect to the average electrostatic potential consistently differ by 0.5–0.6 eV in the two interface components. This difference does not affect the band offsets at the CaF$_2$/Si(111) interface, but leads to different ionization potentials. In this respect, results in the literature for silicon suggest that it is the PBE0(α) scheme that yields a better agreement with the experiment [9,80]. However, PBE0(α) is an empirical scheme and thus remains unsatisfactory. In the presence of increasing support in favor of PBE0(α) [22,80,87], it is legitimate to inquire whether the fully *ab initio* QS$G\tilde{W}$ scheme still misses a crucial ingredient. Grüneis *et al.* proposed to go beyond such a *GW* scheme by including higher-order diagrams [27]. However, such corrections were found to be insignificant for large-gap materials [27] and would thus leave the band edges of CaF$_2$ unaffected. Therefore, it appears clearly at this stage that further investigations are necessary for allowing a consistent picture to emerge.

In the final part of our work, we determined the reduction of the valence-band offsets as a function of the amount of extra fluorine at the interface. Our results are consistent with the experimental characterization and offer an explanation for the large spread in the measured band offsets. The present analysis suggests that the bonding structure at the CaF$_2$/Si(111) interface should be carefully characterized prior to the achievement of benchmark results for the band offsets.

[1] A. Franciosi and C. G. Van de Walle, Surf. Sci. Rep. **25**, 1 (1996).

[2] W. Kohn and L. J. Sham, Phys. Rev. **140**, A1133 (1965).

[3] J. P. Perdew, K. Burke, and M. Ernzerhof, Phys. Rev. Lett. **77**, 3865 (1996).

[4] A. Alkauskas, P. Broqvist, F. Devynck, and A. Pasquarello, Phys. Rev. Lett. **101**, 106802 (2008).

[5] R. Shaltaf, G.-M. Rignanese, X. Gonze, F. Giustino, and A. Pasquarello, Phys. Rev. Lett. **100**, 186401 (2008).

[6] L. Hedin, Phys. Rev. **139**, A796 (1965).

[7] M. van Schilfgaarde, T. Kotani, and S. Faleev, Phys. Rev. Lett. **96**, 226402 (2006).

[8] M. Shishkin, M. Marsman, and G. Kresse, Phys. Rev. Lett. **99**, 246403 (2007).

[9] W. Chen and A. Pasquarello, Phys. Rev. B **92**, 041115(R) (2015).

[10] A. D. Becke, J. Chem. Phys. **98**, 1372 (1993).

[11] J. P. Perdew, M. Ernzerhof, and K. Burke, J. Chem. Phys. **105**, 9982 (1996).

[12] J. Heyd, G. E. Scuseria, and M. Ernzerhof, J. Chem. Phys. **118**, 8207 (2003).

[13] S. Zhang, D. Tománek, S. G. Louie, M. L. Cohen, and M. S. Hybertsen, Solid State Commun. **66**, 585 (1988).

[14] S. B. Zhang, M. L. Cohen, S. G. Louie, D. Tománek, and M. S. Hybertsen, Phys. Rev. B **41**, 10058 (1990).

[15] D. Cociorva, W. G. Aulbur, and J. W. Wilkins, Solid State Commun. **124**, 63 (2002).

[16] M. Grüning, R. Shaltaf, and G.-M. Rignanese, Phys. Rev. B **81**, 035330 (2010).

[17] A. Wadehra, J. W. Nicklas, and J. W. Wilkins, Appl. Phys. Lett. **97**, 092119 (2010).

[18] H.-P. Komsa, P. Broqvist, and A. Pasquarello, Phys. Rev. B **81**, 205118 (2010).

[19] C. Mietze, M. Landmann, E. Rauls, H. Machhadani, S. Sakr, M. Tchernycheva, F. H. Julien, W. G. Schmidt, K. Lischka, and D. J. As, Phys. Rev. B **83**, 195301 (2011).

[20] C. Mitra, B. Lange, C. Freysoldt, and J. Neugebauer, Phys. Rev. B **84**, 193304 (2011).

[21] A. Punya and W. R. L. Lambrecht, Phys. Rev. B **88**, 075302 (2013).

[22] K. Steiner, W. Chen, and A. Pasquarello, Phys. Rev. B **89**, 205309 (2014).

[23] Y. Hinuma, A. Grüneis, G. Kresse, and F. Oba, Phys. Rev. B **90**, 155405 (2014).

[24] A. Alkauskas, P. Broqvist, and A. Pasquarello, Phys. Status Solidi B **248**, 775 (2011).

[25] A. Alkauskas and A. Pasquarello, Phys. Rev. B **84**, 125206 (2011).

[26] W. Chen and A. Pasquarello, Phys. Rev. B **86**, 035134 (2012).

[27] A. Grüneis, G. Kresse, Y. Hinuma, and F. Oba, Phys. Rev. Lett. **112**, 096401 (2014).

[28] W. Chen and A. Pasquarello, Phys. Rev. B **96**, 020101(R) (2017).

[29] P. Broqvist and A. Pasquarello, Microelectron. Eng. **84**, 2022 (2007).

[30] M. A. Olmstead, R. I. G. Uhrberg, R. D. Bringans, and R. Z. Bachrach, Phys. Rev. B **35**, 7526 (1987).

[31] F. J. Himpsel, F. U. Hillebrecht, G. Hughes, J. L. Jordan, U. O. Karlsson, F. R. McFeely, J. F. Morar, and D. Rieger, Appl. Phys. Lett. **48**, 596 (1986).

[32] R. M. Tromp and M. C. Reuter, Phys. Rev. Lett. **61**, 1756 (1988).

[33] J. D. Denlinger, E. Rotenberg, U. Hessinger, M. Leskovar, and M. A. Olmstead, Phys. Rev. B **51**, 5352 (1995).

[34] J. Harada, I. Takahashi, Y. Itoh, N. Sokolov, N. Yakovlev, Y. Shusterman, and J. Alvarez, J. Cryst. Growth **163**, 31 (1996).

[35] A. Klust, M. Bierkandt, J. Wollschläger, B. H. Müller, T. Schmidt, and J. Falta, Phys. Rev. B **65**, 193404 (2002).

[36] C. R. Wang, B. H. Müller, E. Bugiel, and K. R. Hofmann, J. Vac. Sci. Technol. A **22**, 2182 (2004).

[37] C. Deiter, M. Bierkandt, A. Klust, C. Kumpf, Y. Su, O. Bunk, R. Feidenhans'l, and J. Wollschläger, Phys. Rev. B **82**, 085449 (2010).

[38] D. Rieger, F. J. Himpsel, U. O. Karlsson, F. R. McFeely, J. F. Morar, and J. A. Yarmoff, Phys. Rev. B **34**, 7295 (1986).

[39] F. J. Himpsel, U. O. Karlsson, J. F. Morar, D. Rieger, and J. A. Yarmoff, Phys. Rev. Lett. **56**, 1497 (1986).

[40] P. Avouris and R. Wolkow, Appl. Phys. Lett. **55**, 1074 (1989).

[41] A. B. McLean and F. J. Himpsel, Phys. Rev. B **39**, 1457 (1989).

[42] T. F. Heinz, F. J. Himpsel, E. Palange, and E. Burstein, Phys. Rev. Lett. **63**, 644 (1989).

[43] A. Izumi, Y. Hirai, K. Tsutsui, and N. S. Sokolov, Appl. Phys. Lett. **67**, 2792 (1995).

[44] A. V. Krukau, O. A. Vydrov, A. F. Izmaylov, and G. E. Scuseria, J. Chem. Phys. **125**, 224106 (2006).

[45] D. R. Hamann, Phys. Rev. B **88**, 085117 (2013).

[46] M. van Setten, M. Giantomassi, E. Bousquet, M. Verstraete, D. Hamann, X. Gonze, and G.-M. Rignanese, Comput. Phys. Commun. **226**, 39 (2018).

[47] M. Verstraete and X. Gonze, Phys. Rev. B **68**, 195123 (2003).

[48] O. Madelung, *Semiconductors: Data Handbook* (Springer, Berlin, 1996).

[49] M. S. Hybertsen and S. G. Louie, Phys. Rev. B **34**, 5390 (1986).

[50] F. Gygi and A. Baldereschi, Phys. Rev. Lett. **62**, 2160 (1989).

[51] A. Fleszar and W. Hanke, Phys. Rev. B **56**, 10228 (1997).

[52] S. Sharma, J. K. Dewhurst, A. Sanna, and E. K. U. Gross, Phys. Rev. Lett. **107**, 186401 (2011).

[53] Z. H. Levine and D. C. Allan, Phys. Rev. Lett. **63**, 1719 (1989).

[54] S. L. Adler, Phys. Rev. **126**, 413 (1962).

[55] N. Wiser, Phys. Rev. **129**, 62 (1963).

[56] S. Lebègue, B. Arnaud, M. Alouani, and P. E. Bloechl, Phys. Rev. B **67**, 155208 (2003).

[57] X. Gonze, B. Amadon, P.-M. Anglade, J.-M. Beuken, F. Bottin, P. Boulanger, F. Bruneval, D. Caliste, R. Caracas, and M. Côté, Comput. Phys. Commun. **180**, 2582 (2009).

[58] P. Giannozzi, S. Baroni, N. Bonini, M. Calandra, R. Car, C. Cavazzoni, D. Ceresoli, G. L. Chiarotti, M. Cococcioni, and I. Dabo, J. Phys.: Condens. Matter **21**, 395502 (2009).

[59] C. G. Van de Walle and R. M. Martin, Phys. Rev. B **35**, 8154 (1987).

[60] A. Baldereschi, S. Baroni, and R. Resta, Phys. Rev. Lett. **61**, 734 (1988).

[61] W. Chen, G. Miceli, G.-M. Rignanese, and A. Pasquarello, Phys. Rev. Mater. **2**, 073803 (2018).

[62] G. Miceli, W. Chen, I. Reshetnyak, and A. Pasquarello, Phys. Rev. B **97**, 121112(R) (2018).

[63] T. Bischoff, I. Reshetnyak, and A. Pasquarello, Phys. Rev. B **99**, 201114(R) (2019).

[64] T. Tsujibayashi, K. Toyoda, S. Sakuragi, M. Kamada, and M. Itoh, Appl. Phys. Lett. **80**, 2883 (2002).

[65] P. Borlido, M. A. L. Marques, and S. Botti, J. Chem. Theory Comput. **14**, 939 (2018).

[66] H. Zheng, M. Govoni, and G. Galli, Phys. Rev. Materials **3**, 073803 (2019).

[67] T. Bischoff, J. Wiktor, W. Chen, and A. Pasquarello, Phys. Rev. Mater. **3**, 123802 (2019).

[68] F. Kaplan, M. E. Harding, C. Seiler, F. Weigend, F. Evers, and M. J. van Setten, J. Chem. Theory Comput. **12**, 2528 (2016).

[69] R. M. Hazen and L. W. Finger, J. Appl. Crystallogr. **14**, 234 (1981).

[70] K. Shinozaki, T. Honma, K. Oh-ishi, and T. Komatsu, Opt. Mater. **33**, 1350 (2011).

[71] K. Liu, H. Wang, and X. Zhang, *Ductile Mode Cutting of Brittle Materials* (Springer, Berlin, 2020).

[72] C. G. Van de Walle, Phys. Rev. B **39**, 1871 (1989).

[73] E. L. Shirley, Phys. Rev. B **58**, 9579 (1998).

[74] G. W. Rubloff, Phys. Rev. B **5**, 662 (1972).

[75] J. Wiktor, I. Reshetnyak, F. Ambrosio, and A. Pasquarello, Phys. Rev. Mater. **1**, 022401 (2017).

[76] J. Wiktor, U. Rothlisberger, and A. Pasquarello, J. Phys. Chem. Lett. **8**, 5507 (2017).

[77] M. Cardona and M. L. W. Thewalt, Rev. Mod. Phys. **77**, 1173 (2005).

[78] W. R. L. Lambrecht, C. Bhandari, and M. van Schilfgaarde, Phys. Rev. Mater. **1**, 043802 (2017).

[79] J. P. Nery, P. B. Allen, G. Antonius, L. Reining, A. Miglio, and X. Gonze, Phys. Rev. B **97**, 115145 (2018).

[80] W. Chen and A. Pasquarello, Phys. Rev. B **90**, 165133 (2014).

[81] M. Kim, Y.-J. Zhao, A. J. Freeman, and W. Mannstadt, Appl. Phys. Lett. **84**, 3579 (2004).

[82] Y. Ma and M. Rohlfing, Phys. Rev. B **75**, 205114 (2007).

[83] M. Bertocchi, E. Luppi, E. Degoli, V. Véniard, and S. Ossicini, Phys. Rev. B **86**, 035309 (2012).

[84] H. Fujitani and S. Asano, Surf. Sci. **268**, 265 (1992).

[85] S. Ossicini, C. Arcangeli, and O. Bisi, Phys. Rev. B **43**, 9823 (1991).

[86] L. Weston, H. Tailor, K. Krishnaswamy, L. Bjaalie, and C. G. Van de Walle, Comput. Mater. Sci. **151**, 174 (2018).

[87] Z. Guo, F. Ambrosio, W. Chen, P. Gono, and A. Pasquarello, Chem. Mater. **30**, 94 (2018).

[88] S. Satpathy and R. M. Martin, Phys. Rev. B **39**, 8494 (1989).

[89] M. R. Salehpour, S. Satpathy, and G. P. Das, Phys. Rev. B **44**, 8880 (1991).

[90] S. Picozzi, S. Massidda, A. Continenza, and R. Resta, Phys. Rev. B **55**, 16318 (1997).

[91] M. A. Olmstead, R. I. G. Uhrberg, R. D. Bringans, and R. Z. Bachrach, J. Vac. Sci. Technol. **4**, 1123 (1986).

[92] F. Xu, M. Vos, and J. H. Weaver, Phys. Rev. B **39**, 8008 (1989).